

A Damage Mechanics Approach to Modeling Permeability Enhancement in Thermo-Hydro-Mechanical Simulations

Justin Pogacnik¹, Mike O'Sullivan and John O'Sullivan

Department of Engineering Science, University of Auckland, Level 3, 70 Symonds St, Auckland 1142, New Zealand

¹j.pogacnik@auckland.ac.nz

Keywords: damage mechanics, permeability enhancement, thermo-hydro-mechanical modeling, cold water injection, finite element method.

ABSTRACT

In geothermal energy production, permeability can be enhanced or inhibited over time by various multi-physics controlled processes such as chemical species dissolution and precipitation, changes in stress or pore pressure, and by temperature effects such as thermal cracking. A wide range of methods has been used to numerically simulate permeability enhancement. Models based on damage mechanics, discrete fracture mechanics, critical shear strain criteria, effective stress, and even empirical permeability multipliers have been proposed in the literature. Damage mechanics offers a way forward that encompasses micro-crack physics while allowing for a realistic description of complex fracture networks. This work seeks to apply a new damage mechanics model that includes Thermal-Hydrological-Mechanical (THM) effects in simulations of thermal cracking problems that are of significance in geothermal energy production. To this end, the damage model was implemented into a fully coupled THM finite element code. This approach allows for the macro-scale representation of complex micro-scale phenomena and offers a natural framework for the investigation of the degree of numerical coupling required for the strong feedback permeability mechanisms involved in the stimulation of permeability.

1. INTRODUCTION AND BACKGROUND

Permeability is one of the most crucial hydrologic parameters and can fluctuate up to 16 orders of magnitude (Ingebritsen *et al.* (2006)). Permeability often determines the feasibility of projects involving geologic processes and their economic potential. This is especially true in geothermal energy production. Permeability should be regarded as a time-dependent property that can be enhanced or inhibited over time by various processes such as chemical species dissolution and precipitation, changes in stress or pore pressure, and by temperature effects such as thermal cracking. If permeability is too low, then a geothermal well is often stimulated by over pressurization (hydrofracking or hydroshearing) or injection of cold water to induce thermal cracking and thus enhancing permeability.

Clark (1949) published perhaps the first paper on hydraulic fracturing (hydrofracking). The oil industry had long recognized the need to increase well productivity. The basic process required that a viscous liquid carrying granular material be injected at high pressure to fracture the rock formation. The granular material (usually sand) then acted as a propping agent to hold the newly created fracture(s) open. Hydrofracking was originally termed "Pressure Parting" since it was thought that the fluid used in the process required pressurization to a level higher than the overburden pressure to part the formation. Clark (1949) reported that 50% of wells showed an increase in production when hydrofracking was performed.

Since Clark's work, well stimulation has become commonplace. We now know that hydrofracking occurs when injection pressure exceeds the minimum principal stress. This opens fractures in tension and results in the opening of highly permeability fracture pathways. However, in the geothermal sector, the goal of stimulation is not to solely increase fluid flow. If cold fluid travels too quickly through a medium, then it does not have sufficient time to pick up the heat necessary for efficient energy extraction. There is a growing interest in investigating the possibility of hydroshearing for geothermal well stimulation for just this reason. The term hydroshearing was coined by Cladouhos, *et al.* (2009) to indicate that existing fractures dilate and slip in shear at lower pressures than are required by hydrofracking.

A number of works have been published that present coupled multiphysics simulations of both hydrofracking and hydroshearing. Some of the hydrofracking studies include models based on damage mechanics such as Zhou, *et al.* (2006) and Lu, *et al.* (2013). These papers present a coupled hydro-mechanical framework to test damage-induced permeability enhancement models for application to shale oil plays. A noticeable shortcoming in these approaches (for geothermal) is a lack of consideration of thermal effects as well as non-tensile fracture scenarios such as hydroshearing. More recent examples of shear stimulation simulations with geothermal applications can be seen in the works of Kelkar, *et al.* (2012), Rutqvist, *et al.* (2013), and Dempsey, *et al.* (2013). Rutqvist, *et al.* (2013) used a simplified Coulomb criterion to determine the volume that would be enhanced by shear failure near an injection site. The initiation criterion was simplified so that it effectively became a maximum principal stress criterion. Their work targeted pre-stimulation behavior, so permeability evolution was not taken into account. Kelkar, *et al.* (2012) and Dempsey, *et al.* (2013) used a Mohr-Coulomb initiation criterion to determine where shear slip occurred near an injection site. Permeability was then altered by either a multiplier (Kelkar, *et al.* (2012)) or by a sigmoidal function (Dempsey, *et al.* (2013)), both designed to approximate the measured permeability data obtained by Lee and Cho (2002). There are also a number of models that use an approach for simulating permeability enhancement by specifying permeability as a function of effective stress (Nathenson (1999) and Pogacnik, *et al.* (2012)). Both the effective stress relationships of Nathenson (1999) and the sigmoidal relationship of Lee and Cho (2002) can trace their roots back to the cubic law of planar fracture flow popularized by Gangi (1978). While the law theoretically describes flow through a single channel, it often breaks down in complex flow regimes with multiple nonlinear fracture pathways. The present work seeks to model permeability enhancement from permeability-strain relationships derived from

intact samples tested in the works of Wang and Park (2002); Tang, *et al.* (2002); Zhou, *et al.* (2006); and Zhang, *et al.* (2013) that do not rely on the cubic law that describes fluid flow through a single planar channel.

In this work we apply an isotropic damage mechanics model in a fully coupled THM finite element code in order to simulate the effects of cold-water injection. We test a number of damage initiation criteria and learn that the criterion chosen can drastically affect the resulting area/volume of rock stimulated. We present the theory, methodology of implementation, model calibration, and results for a 2-D cold-water injection scenario. This work is a necessary first step in developing damage mechanics models for use in geothermal applications.

2. BALANCE EQUATIONS

2.1 Linear Momentum Balance for the Rock Matrix

In this work, inertial forces in the solid rock matrix were ignored. The linear momentum balance from Bonet and Wood (2008) is written as:

$$\text{div}\boldsymbol{\sigma} + \mathbf{f} = \mathbf{0} \quad (1)$$

where the vector $\text{div}\boldsymbol{\sigma}$ is the spatial divergence of the Cauchy stress tensor (to be formally defined in the next section) and \mathbf{f} a vector of body forces (both external and density related). Note that boldface fonts are used to express matrix and vector quantities. The Cauchy stress can be split into two components to represent the effect of pore fluid pressure on the solid matrix (Lewis and Schrefler (1998); Ingebritsen, Sanford, and Neuzil (2006)):

$$\boldsymbol{\sigma} = \boldsymbol{\sigma}'' - \alpha p \mathbf{I} \quad (2)$$

where $\boldsymbol{\sigma}''$ is Biot's effective stress tensor, α is a constant between 0 and 1, p is the pore fluid pressure, and \mathbf{I} is the identity tensor. The effective stress is defined by

$$\boldsymbol{\sigma}'' = \mathbf{C}^D : (\boldsymbol{\varepsilon} - \boldsymbol{\varepsilon}_T) \quad (3)$$

where \mathbf{C}^D is the fourth order material constitutive tensor (to be defined in the next section), $\boldsymbol{\varepsilon}$ is the strain tensor, “:” represents the double contraction of two tensors, and $\boldsymbol{\varepsilon}_T$ is the thermal strain tensor given by

$$\boldsymbol{\varepsilon}_T = \left(\frac{\beta_s}{3} \right) (\Delta T) \mathbf{I} \quad (4)$$

where β_s is the volumetric coefficient of thermal expansion of the solid and ΔT is the change in temperature from the reference state.

2.2 Mass Balance

The pore fluid is assumed to be single phase and consist of fully saturated pure water in this work. The fluid balance equation can be written (from Lewis and Schrefler (1998)):

$$0 = -((1-n)\beta_s + n\beta_w) \frac{\partial T}{\partial t} + \left(\frac{1-n}{K_s} + \frac{n}{K_w} \right) \frac{\partial p}{\partial t} + \nabla \cdot \mathbf{v}^s + \nabla \cdot \left\{ \frac{\boldsymbol{\kappa}}{\mu_w} [-\nabla p + \rho_w \mathbf{g}] \right\} - Q_p \quad (5)$$

where the subscripts s and w refer to the solid and fluid components respectively, t is time, n is the porosity, K are the bulk moduli, \mathbf{v}^s is the velocity of the solid components, $\boldsymbol{\kappa}$ is the permeability tensor, μ_w is the fluid viscosity, ρ_w is the fluid density, \mathbf{g} is the gravity acceleration vector, and Q_p represents fluid mass flow into the system. The derivation of (5) assumes linear dependence of porosity, rock density, and fluid density on pressure and temperature.

2.3 Energy Balance

Lastly, to couple thermal effects, we introduce the energy balance equation, also from Lewis and Schrefler (1998):

$$\left(\rho_w C_w + C_s \rho_s \right) \frac{\partial T}{\partial t} + \rho_w C_w \frac{\boldsymbol{\kappa}}{\mu_w} (-\nabla p + \rho_w \mathbf{g}) \cdot \nabla T - \nabla \cdot \{ \boldsymbol{\chi} \cdot \nabla T \} = 0 \quad (6)$$

where C represents the specific heat, T is the temperature, ρ_s is the density of the solid, and $\boldsymbol{\chi}$ is the effective thermal diffusivity of the saturated medium. In (6), fluid viscosity and density were taken to be dependent on temperature only, unless the heat and mass transfer simulation was performed with TOUGH2, and then the appropriate properties were determined by the equation of state used in the simulation. We know that parameters such as permeability and Cauchy stress depend upon the deformation state of the material. One possible theoretical framework for capturing this dependency is damage mechanics. The necessary details for this work will be discussed in the next section.

3. CONSTITUTIVE MODEL

3.1 Introduction

Voyiadjis and Kattan (2005) describe damage as the process of the initiation and growth of micro-cracks and cavities. At the micro-scale, these phenomena are discontinuous. They credit Kachanov with the introduction of a continuous damage variable describe the density of micro-scale defects and their effect at the macro-scale. Damage could be considered as a deterioration process similar to irreversible strain (Besson *et al.* (2010)). The damage variable is written in terms of stress or strain and can be used in solid mechanics analyses to predict the initiation of macro-cracks. These cracks can affect a variety of parameters including, but not limited to, material stiffness and permeability.

3.2 Stress-Strain Constitutive Relationship

Stresses result in deformation (strain) of a solid body. The relationship between stress and strain is called a constitutive relationship. A strain energy density function serves as the starting point of constitutive model development and describes the work done by stresses to deform a body from the initial configuration to the deformed configuration. The simplest form of the strain energy density function is the St. Venant-Kirchhoff model:

$$\Psi(\boldsymbol{\varepsilon}) = \frac{1}{2} \lambda \text{tr}(\boldsymbol{\varepsilon})^2 + \eta \boldsymbol{\varepsilon} : \boldsymbol{\varepsilon} \quad (7)$$

where λ and η are the Lamé parameters (related to Young's modulus and Poisson's ratio) and $\text{tr}(\cdot)$ is the trace of a tensor. Taking the first derivative of the strain energy density function with respect to strain yields the Cauchy stress.

$$\boldsymbol{\sigma} = \frac{\partial \Psi}{\partial \boldsymbol{\varepsilon}} = \lambda \text{tr}(\boldsymbol{\varepsilon}) \mathbf{I} + 2\eta \boldsymbol{\varepsilon} \quad (8)$$

The derivative of the Cauchy stress equation with respect to strain yields the fourth-order stiffness tensor, or more properly, the Lagrangian elasticity tensor. In indicial notation, the form of the elasticity tensor is

$$C_{IJKL}^e = \frac{\partial \sigma_{IJ}}{\partial \varepsilon_{KL}} = \frac{\partial^2 \Psi}{\partial \varepsilon_{IJ} \partial \varepsilon_{KL}} = \lambda \delta_{IJ} \delta_{KL} + \eta (\delta_{IK} \delta_{JL} + \delta_{IL} \delta_{JK}) \quad (9)$$

where δ_{IJ} is Kronecker's delta equal to 1 when $I=J$ and equal to 0 when $I \neq J$. In small strain theory, (9) is the standard relation for linear elasticity and in finite strain theory the constitutive model describes a St. Venant-Kirchhoff material. In the case without damage, (9) can be used for \mathbf{C}^D in (3) to compute the Cauchy stress in a THM problem.

3.3 Constitutive Relationship with Damage

The first step in damage mechanics is to define the damage variable. De Borst, et al. (2012) state that the damage variable could be defined by a scalar, a second-order tensor, or a fourth-order tensor. In this work, we define damage as a second-order tensor. This allows for either isotropic or anisotropic damage descriptions and is relatively easy to implement and computationally inexpensive. The damage tensor is defined by

$$\mathbf{D} = \sum_k d_k(\cdot) \mathbf{n}_k \otimes \mathbf{n}_k \quad (10)$$

where $d_k(\cdot)$ is a dimensionless scalar function between 0 and 1 proportional to the amount of theoretical microcracking in a representative volume element. If an element is completely intact without damage, $d_k = 0$; in the completely damaged case, $d_k = 1$. There are several options for the functional definition of d_k and this work seeks to investigate some different choices (presented in the next section). In (10), \mathbf{n}_k are normal vectors and \otimes denotes the dyadic or tensor product of the two vectors.

Perhaps Halm and Dragon (1996) were the first to formulate a consistent expression for the strain energy density as a function of damage:

$$\Psi(\boldsymbol{\varepsilon}, \mathbf{D}) = \frac{1}{2} \lambda \text{tr}(\boldsymbol{\varepsilon})^2 + \eta \boldsymbol{\varepsilon} : \boldsymbol{\varepsilon} + G \boldsymbol{\varepsilon} : \mathbf{D} + A \text{tr}(\boldsymbol{\varepsilon}) \boldsymbol{\varepsilon} : \mathbf{D} + 2B(\boldsymbol{\varepsilon} : \boldsymbol{\varepsilon}) : \mathbf{D} \quad (11)$$

Notice that the first two terms are equivalent to the strain energy density from equation (7). In (11), A and B are supplementary constants related to moduli degradation due to damage and G is a constant governing residual damage effects. Determination of the Cauchy stress relation by (8) gives

$$\boldsymbol{\sigma} = \lambda \text{tr}(\boldsymbol{\varepsilon}) \mathbf{I} + 2\eta \boldsymbol{\varepsilon} + G \mathbf{D} + A [\text{tr}(\boldsymbol{\varepsilon} \mathbf{D}) \mathbf{I} + \text{tr}(\boldsymbol{\varepsilon}) \mathbf{D}] + 2B(\boldsymbol{\varepsilon} \mathbf{D} + \mathbf{D} \boldsymbol{\varepsilon}) \quad (12)$$

The effect of G on the permanent deformation upon unloading and subsequent compressive loading is made clear in Figure 1. Also, note that the softening response of the stress-strain graph is controlled by the interactions of the parameters A and B .

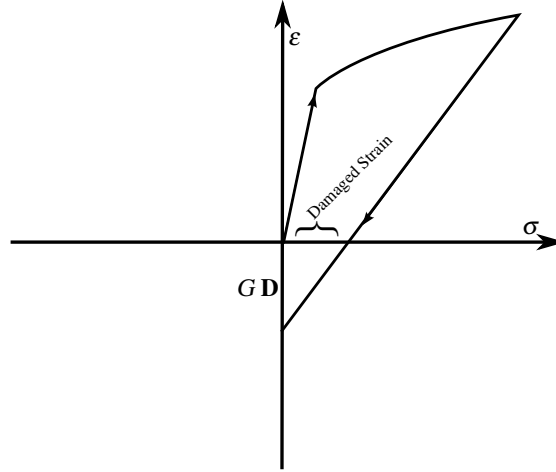


Figure 1. Plot of residual stress for uniaxial tension (adapted from Halm and Dragon (1996)). The stress response softens during loading due to increasing damage. When the load is removed, a permanent strain is left represented as a damage state. Continued compressive loading results a stress state equal to GD at zero strain.

Application of the derivative of (9) to either (11) or (12) yields the equation for the fourth-order elasticity tensor:

$$C_{IJKL}^D = \lambda \delta_{IJ} \delta_{KL} + \eta (\delta_{IK} \delta_{JL} + \delta_{IL} \delta_{JK}) + A (\delta_{IJ} D_{KL} + D_{IJ} \delta_{KL}) + B (\delta_{IK} D_{JL} + \delta_{IL} D_{JK} + D_{IK} \delta_{JL} + D_{IL} \delta_{JK}) \quad (13)$$

The next section will describe the evolution relationships for the damage tensor \mathbf{D} investigated in this work.

4. DAMAGE EVOLUTION

Zhou, *et al.* (2006), explain that, while not entirely rigorous, damage evolution laws are typically taken to be functions of either stress or strain. In this work, we test some functions of each. In the strain-dependent category, we test a criterion call the “energy measure” criterion (De Borst, *et al.* (2012)) based on the strain energy and originally designed for metal plasticity. We also test a strain-dependent criterion by Mazars and Pijauder-Cabot (1989) that was designed for brittle materials such as rock and concrete. In the stress-dependent category, we test a simple maximum principal stress criterion and the well-attested Drucker-Prager yield condition. The Drucker-Prager condition is simply an elliptical version of the Mohr-Coulomb criterion that is more stable in stress regimes where it is not certain that pure shear controls yield and failure.

4.1 Strain-Controlled Evolution

For strain-controlled damage evolution, we first define a damage loading function f that is a function of strain and damage:

$$f(\tilde{\epsilon} - k) = \tilde{\epsilon} - k \quad (14)$$

where $\tilde{\epsilon}$ is a scalar function of the strain tensor and k is the internal variable that specifies a damage threshold value for the scalar strain function. That is, on the yield/failure surface, $f=0$. From De Borst, *et al.* (2012), the energy measure defines the scalar strain function as

$$\tilde{\epsilon} = \sqrt{\frac{1}{E} \boldsymbol{\epsilon} : \mathbf{C}^e : \boldsymbol{\epsilon}} \quad (15)$$

where E is Young's modulus. This energy release rate formula gives equal weight to the tensile and compressive strains making it a poor choice for quasi-brittle materials such as rock. Mazars and Pijauder-Cabot (1989) developed a more suitable definition of the scalar strain function for concrete and rock-like materials:

$$\tilde{\epsilon} = \sqrt{\sum_{i=1}^e \langle \epsilon_i \rangle^2} \quad (16)$$

where the $\langle x \rangle$ are MacAulay brackets defined as

$$\langle \epsilon_i \rangle = \frac{|\epsilon_i| + \epsilon_i}{2} \quad (17)$$

where ε_i are the principal strains. This function results in a value of $\langle \varepsilon_i \rangle = \varepsilon_i$ when positive (tension) and $\langle \varepsilon_i \rangle = 0$ when negative (compression).

4.2 Stress-Controlled Evolution

For stress-controlled damage evolution, the same process was followed as in the strain-controlled case, with the exception of the introduction of a scalar stress variable $\tilde{\sigma}$. The first criterion tested was simple maximum principal stress criterion:

$$\tilde{\sigma} = \max(\sigma_i) \quad (18)$$

In this case, (similarly to (16)) a tensile condition is required for damage to occur. Real materials, however, rarely display failure criteria reliant only upon the maximum principal stress. A more realistic stress-based criterion used in this work was the Drucker-Prager criterion as outlined in Chen and Han (1995). The Drucker-Prager condition is a popular and robust yield criterion for quasi-brittle materials like rocks and concrete that is related to the Mohr-Coulomb yield criterion. The scalar stress variable is defined as

$$\tilde{\sigma} = \alpha I_1 + \sqrt{J_2} \quad (19)$$

where I_1 is the first invariant of the stress tensor and J_2 is the second invariant of the deviatoric stress tensor. The deviatoric stress tensor is composed of the shear terms of the Cauchy stress tensor and is defined as

$$\mathbf{S} = \boldsymbol{\sigma} - \frac{1}{3} \text{tr}(\boldsymbol{\sigma}) \mathbf{I} \quad (20)$$

The first invariant of the stress tensor is defined as

$$I_1 = \sigma_1 + \sigma_2 + \sigma_3 \quad (21)$$

The second invariant of the deviatoric stress tensor is defined as

$$J_2 = S_1 S_2 + S_1 S_3 + S_2 S_3 = \frac{1}{3} (I_1)^2 - I_2 \quad (22)$$

In (19), the variable α is a material constant related to the internal angle of friction (also used in a Mohr-Coulomb condition).

$$\alpha = \frac{2 \sin \theta}{\sqrt{3} (3 - \sin \theta)} \quad (23)$$

When $\alpha = 0$, the Mohr-Coulomb condition is recovered. In this work, for the 2D analyses performed, the third principal stress was set to zero, i.e., $\sigma_3 = 0$.

4.3 Damage Calculation

For both the strain- and stress-controlled cases, damage was computed as a piecewise function of the scalar variable \tilde{x} , where x was either ε or σ . Damage was globally set to zero at the start of a simulation. At the end of each time step, the scalar variable was computed. If the scalar value was over the critical value \tilde{x}_c , damage linearly increased until a maximum value \tilde{x}_{off} , was reached.

The values of \tilde{x}_c and \tilde{x}_{off} were chosen by fitting the experimental data presented in Sections 6.2 and 6.3. The material constitutive law naturally hardens at higher strains. Therefore, damage was set to increase in such a way that uniaxial stress remained constant at values of the scalar variable over the cutoff value in equation (24). Figure 2 displays damage as a function of the normalized scalar variable. The specification of the increase in damage after the cutoff value results in the stress plateau seen in Figure 3 below.

$$D^i = \begin{cases} 0 & \text{if } \tilde{x} < \tilde{x}_c \\ \frac{D_{\text{max}}}{\tilde{x}_{\text{off}} - \tilde{x}_c} \tilde{x} - D_{\text{max}} \frac{\tilde{x}_c}{\tilde{x}_{\text{off}} - \tilde{x}_c} & \text{if } \tilde{x}_c \leq \tilde{x} \leq \tilde{x}_{\text{off}} \\ 1 - (1 - D_{\text{max}}) \frac{\tilde{x}_{\text{off}}}{\tilde{x}} & \text{if } \tilde{x} > \tilde{x}_{\text{off}} \end{cases} \quad (24)$$

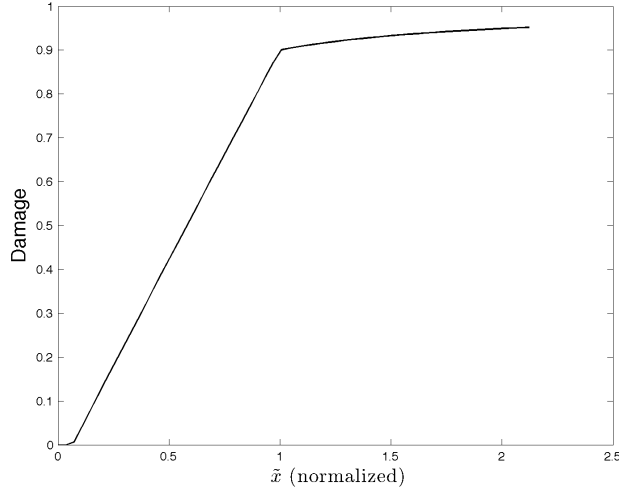


Figure 2. Damage as a function of the normalized scalar strain variable ($\tilde{\epsilon}$).

5. PERMEABILITY ENHANCEMENT

There is some data in the literature that seeks to characterize permeability as a function of strain, based on experiments. Most of that work is related to the “cubic law” and flow through single fractures, e.g., Gangi (1978) or Witherspoon (1980). There are very few studies that characterize bulk permeability as a function of bulk deformation. A few examples of this type of work can be seen in Wang and Park (2002); Tang, *et al.* (2002); Zhou, *et al.* (2006); and Zhang, *et al.* (2013) – all of which tested different sandstone samples. Those works report permeability values with some variability, e.g., the maximum permeability reported is of the order of 1e-18, 1e-16, 1e-13, and 1e-17 m², respectively. A subsequent model calibration was performed based on the normalized permeability-strain curves. The value of permeability was then scaled to be realistic for a representative geothermal rock.

As a starting point for this work, we chose to cast permeability as a function of damage, instead of stress or strain. This enabled a consistent permeability evolution calculation to be performed regardless of the damage evolution criterion used. The permeability function used in this work was

$$\boldsymbol{\kappa}(\mathbf{D}) = \boldsymbol{\kappa}_0 + \boldsymbol{\kappa}_1^i(\mathbf{D})\mathbf{I} - \boldsymbol{\kappa}_2^i(\mathbf{D})\mathbf{I} \quad (25)$$

where $\boldsymbol{\kappa}_0$ is the initial (potentially anisotropic) permeability tensor with individual components κ_0^x , κ_0^y , and κ_0^z . The functions $\boldsymbol{\kappa}_1$ and $\boldsymbol{\kappa}_2$ are sigmoidal functions designed to capture permeability changes with damage qualitatively similar to the behavior seen in Figure 2.

$$\boldsymbol{\kappa}_1^i = \frac{\boldsymbol{\kappa}_{\max} - \boldsymbol{\kappa}_0^i}{1 + \exp\left[-\nu_1\left(D^i - D_1\right)\right]} \quad (26)$$

$$\boldsymbol{\kappa}_2^i = \frac{\boldsymbol{\kappa}_{\max} - \boldsymbol{\kappa}_f}{1 + \exp\left[-\nu_2\left(D^i - D_2\right)\right]} \quad (27)$$

In equations (26) and (27), the superscript $i = x, y, \text{ or } z$. Therefore, damage could be anisotropic. The parameters $\boldsymbol{\kappa}_{\max}$, $\boldsymbol{\kappa}_0$, $\boldsymbol{\kappa}_f$, ν_1 , ν_2 , D_1 , and D_2 are curve fit parameters that are adjusted according to available experimental data. The process of fitting permeability to the data will be outlined in the next section.

6. MODEL CALIBRATION

In order to model permeability enhancement at the finite element mesh scale, it is first necessary to calibrate the numerical model with some known data. While there is little laboratory data that studies the relationship between the stress-strain state and permeability, some work has been performed on brittle reservoir sedimentary rocks. Examples of these exercises can be seen in Wang and Park (2002); Tang, *et al.* (2002); Zhou, *et al.* (2006); and Zhang, *et al.* (2013).

6.1 Mechanical Behavior of Fractured Rock

Bieniawski (1970) provided an in-depth analysis of the time-dependent stress-strain behavior of fractured sandstone rocks. Figure 2 displays an idealized adaptation of the stress-strain and permeability-strain response figure from that work and the work of Zhang *et al.* (2013). In the figure, the solid line represents the stress-strain response and the dashed line represents the permeability-strain response of a fractured sandstone specimen loaded in compression. Strain equal to A represents an initial “toe-in” region of the stress-strain curve (terminology from ASTM standards) that is indicative of slack coming out of the system and initially large pore space closing under compression. B represents the elastic deformation portion of loading and typically shows little change in permeability. C is the onset point of damage where material properties begin to rapidly change (including permeability). After the

peak stress or rock strength, D, Zhang *et al.* (2013) explain that E represents a turning point in the stress-strain curve and is typically the strain value where peak permeability occurs. The next sections describe modeling experiments seeking to match the stress-strain and permeability-strain data from experimental data.

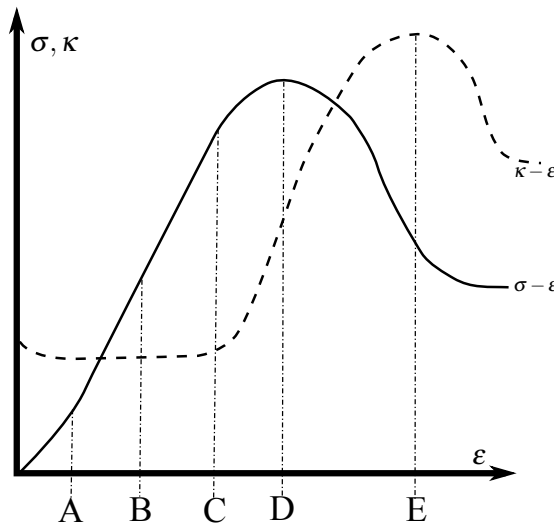


Figure 3. Idealized stress-strain and permeability-strain curves for fractured sandstone samples (adapted from Zhang, *et al.* (2013)).

6.2 Stress-Strain Behavior

Bieniawski (1970) reports that the stress-strain behavior of fractured limestone samples in compression is highly dependent upon the strain rate. However, the model used in this work, based on from equation (12) is not time-dependent. For calibration of the stress-strain curve, we used compression test data from Wang and Park (2002), Zhou, *et al.* (2006), and Zhang, *et al.* (2013). Figure 3 displays the calibrated stress-strain result using the Mazars/Pijauder-Cabot initiation criterion of the strain-controlled case. A similar curve was obtained for the energy measure criterion. The stress-controlled cases match the stress-strain data well until strain is about 1%.

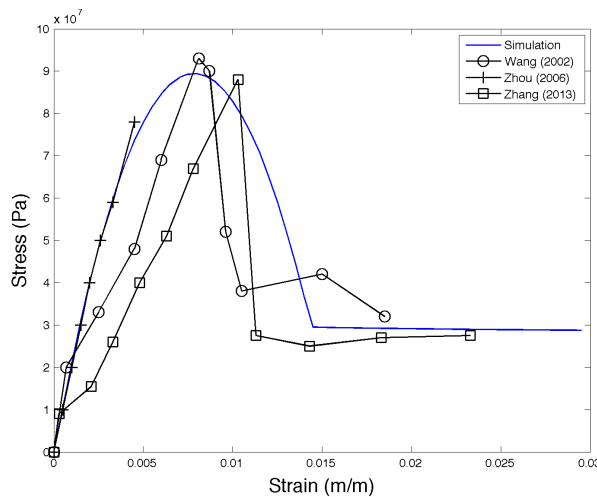


Figure 4. Stress-strain behavior of calibrated model compared to literature data for compression tests on fractured sandstone samples. This figure displays the result for Mazars and Pijauder-Cabot criterion of the strain-controlled case.

In this analysis, parameter G of (12) was chosen to be equal to zero. This simplifies the expression for Cauchy stress, but is only valid if no unloading occurs during simulations. The parameters A and B were then chosen to be equal to $\lambda/2$ and $\eta/2$, respectively. An inspection of (12) shows that in the fully damaged case ($\mathbf{D}=\mathbf{I}$), the Cauchy stress will be zero. This ensures that the stress state will be consistent with the mode of loading. Some choices of A and B can result in the stress response softening to the point that the curve passes the horizontal axis and moves into a different stress regime. For example, a tensile test softens when damage occurs; it could soften to a point that the predicted stress of a model actually goes negative (compressive).

We independently sought to match the data from Figure 3, but found that the choice for Young’s modulus ($E=20.3$ MPa) and Poisson’s ratio ($\nu=0.2$) from Zhou, *et al.* (2006) provide a good fit to the data for all the evolution criteria. The other damage evolution relevant parameters are summarized in Table 1 at the end of this section.

6.3 Permeability-Strain Behavior

Permeability was fit as closely as possible to the data presented in Wang and Park (2002); Tang, *et al.* (2002); and Zhang, *et al.* (2013) by adjusting the constants in equations (25)-(27). Under the current formulation, permeability evolution is not reversible. It is desirable to formulate a permeability evolution relationship that shows an appropriate increase in permeability with applied load, but then some reversibility when the load is removed. Developing a model that matches this behavior is a work in progress. As mentioned earlier, there was a large discrepancy in permeability data for coarse sandstones in the previous work. In order to calibrate the model, all the permeability values were normalized to the maximum permeability of each sample, then qualitatively calibrated based on those results. For this work, we set $\kappa_0 = 1.0\text{e-}16 \text{ m}^2$, $\kappa_{\text{max}} = 5.0\text{e-}15 \text{ m}^2$, and $\kappa_f = 4.0\text{e-}15 \text{ m}^2$. Figure 5 displays the results for the permeability evolution of this model with the normalized permeability from the experimental works mentioned.

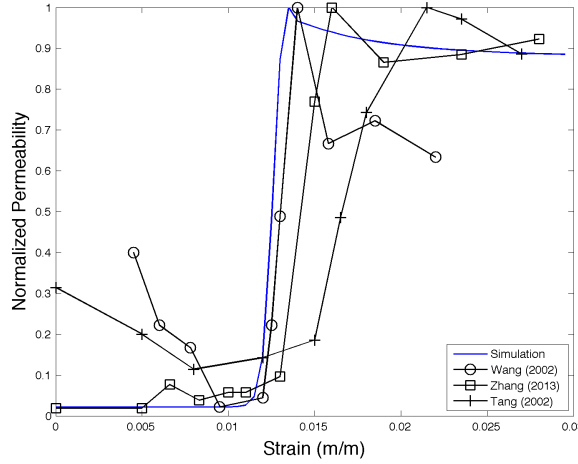


Figure 5. Permeability-strain behavior of calibrated model compared to literature data for compression tests on fractured Sandstone samples. This figure displays the result for Mazars and Pijauder-Cabot criterion of the strain-controlled case.

In order to match the permeability evolution to the experimental data, the parameters ν_1 , ν_2 , D_1 , and D_2 were adjusted accordingly. Table 1 displays the results for each parameter for each initiation/evolution criterion.

Table 1. Parameters used for each damage model evolution criterion in this work.

| Param \ Model | Energy Measure | Mazars/Pijauder-Cabot | σ_{max} | Drucker-Prager |
|-----------------------------|-----------------------|------------------------------|---|-----------------------|
| \tilde{x}_c | 0.0002 | 0.0002 | 5.0e6 | 5.0e6 |
| \tilde{x}_{off} | 0.015 | 0.003 | 1.5e8 | 3.3e7 |
| ν_1 | 50 | 50 | 50 | 50 |
| ν_2 | 50 | 50 | 50 | 50 |
| D_1 | 0.81 | 0.81 | 0.65 | 0.6 |
| D_2 | 0.9 | 0.9 | 0.72 | 0.72 |

7. SIMULATION SET-UP

A 2-D hydraulic stimulation problem similar to an example from Lu, *et al.* (2013) was set up. The geometry tested represented a cross section through a vertical borehole drilled into a homogenous isotropic medium subject to an anisotropic stress state. The maximum principal stress component was denoted as σ_1 and the minimum principal stress component as σ_3 . The geometry was a half-symmetric rectangular area 200x100 mm with a half borehole of 10 mm diameter halfway along the bottom edge. The boundary conditions correspond to a roller along the left and bottom edges; σ_1 prescribed on the right edge; σ_3 prescribed on the top edge; and pressure and temperature prescribed on the left, top, and right edges. Cold water was injected from the borehole at a given pressure over the hydrostatic initial pressure. Figure 6 displays the finite element mesh geometry used with boundary conditions and Table 2 displays the material parameters used in this work.

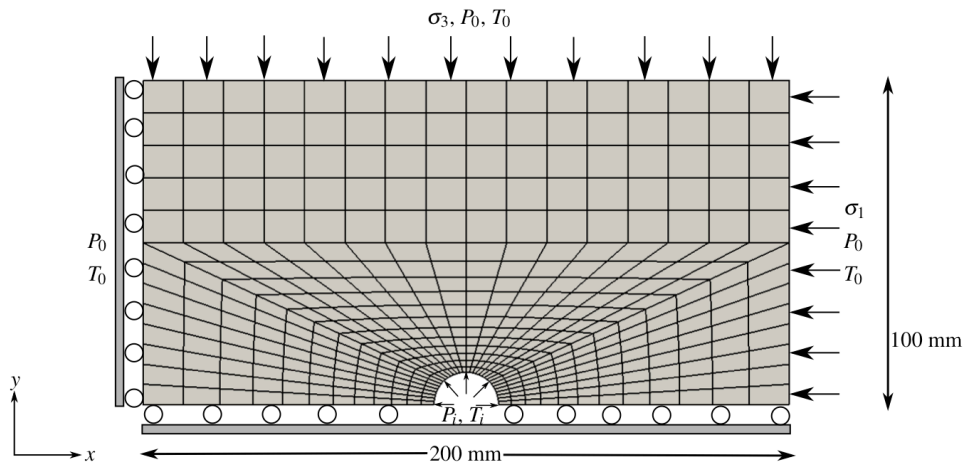


Figure 6. Geometry and finite element mesh used in this work. Adapted from Lu, *et al.* (2013).

Table 2. Values of material parameters used.

| Parameter | Symbol | Value | Units |
|--|-----------|----------|-------------------|
| Young's modulus | E | 20.3E+9 | Pa |
| Poisson's ratio | ν | 0.2 | - |
| solid density | ρ^s | 2500 | kg/m ³ |
| porosity | n | 1.00E-01 | - |
| permeability | κ | 1.00E-16 | m ² |
| fluid bulk modulus | K_w | 3.30E+09 | Pa |
| solid coefficient of thermal expansion | β_s | 1.77E-06 | 1/°C |
| fluid coefficient of thermal expansion | β_w | 2.02E-04 | 1/°C |
| solid specific heat | C_s | 840 | J/(kg °C) |
| fluid specific heat | C_w | 4187 | J/(kg °C) |

The boundary conditions were set to be an approximation of conditions at 1000 m depth in a geothermal field. σ_1 and σ_3 were set to be 25 MPa and 12.5 MPa (compression), respectively. The initial pore fluid pressure P_0 was set to 10 MPa and the initial temperature T_0 was 200° C. The simulation was run with those conditions to a “natural state” for a simulated time of 10E6 sec. At that point, there was no further change in the unknown variables: displacement, temperature, and fluid pressure. Cold fluid injection of 100° C water began at $t = 0$ s after the natural state at a pressure of 8 MPa. The injection pressure was increased every 500 sec by 10% until a maximum injection pressure of 15.6 MPa was reached after 3500 sec. Figure 7 displays the injection pressure as a function of time.

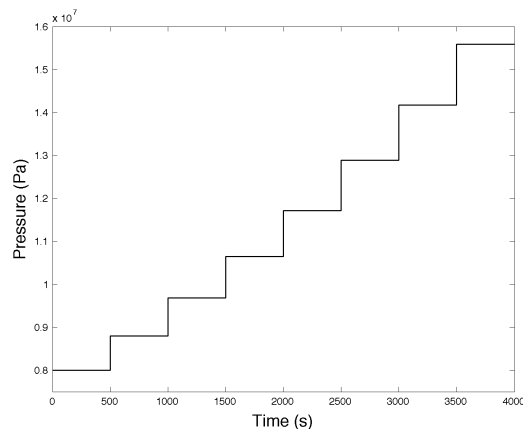


Figure 7. Injection pressure as a function of time for the cold-water injection simulations performed in this work. After 2500 s, the injection pressure is greater than the minimum principal stress σ_3 .

8. RESULTS AND DISCUSSION

In the 2-D injection simulations performed in this work, damage was initially set to zero everywhere. It was found that the addition of the borehole significantly changes the stress state and damage state of the material. This is expected behavior and consistent with linear elastic fracture mechanics (Inglis (1913)). Figure 8 displays the results for damage around the borehole before any injection.

Any damage is a result only of the *in situ* stress/strain state and the stress/strain concentrations that result around a circular flaw. That figure highlights the difference between various initiation criteria. Recall that all the models were first calibrated to compression stress-strain and permeability-strain relationships. Figure 9 displays the damage around the borehole for time = 4000s (at the end of the simulation). Cold-water injection has increased the damage around the borehole. The maximum principal stress (top-left) and Mazars/Pijauder-Cabot (bottom-right) show a classic “butterfly” shape in the damage field. This is typical of mode I fracture mechanics analyses and expected behavior in the failure of many materials. Although it was not obvious that this may be an outcome in a borehole pressurization scenario. The behavior of the Drucker/Prager (bottom-left) model is perhaps more expected. The damage initiates in the area of highest shear stress near the stress concentration. However, during injection, damage appears to be increased horizontally in the direction of the maximum principal stress, which implies an opening in the direction of the minimum principal stress. The energy measure criterion (top-right) predicted very little damage during injection, but the damage did predominately occur in the same direction as the Drucker/Prager condition.

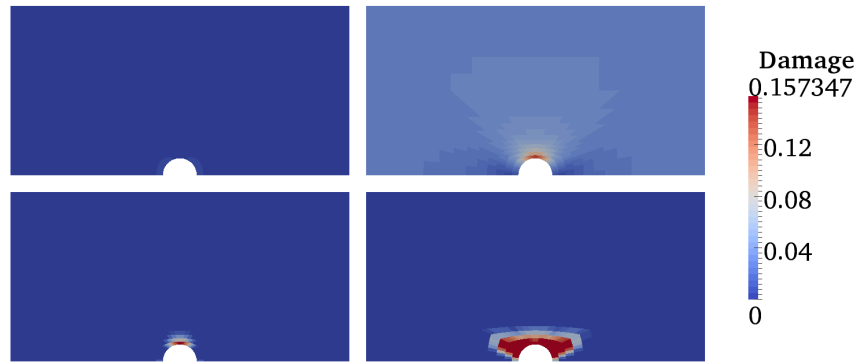


Figure 8. Damage around a borehole prior to injection for the different initiation criteria. From bottom-left moving clockwise, the criteria are: Drucker/Prager, maximum principal stress, energy measure, and Mazars/Pijauder-Cabot.

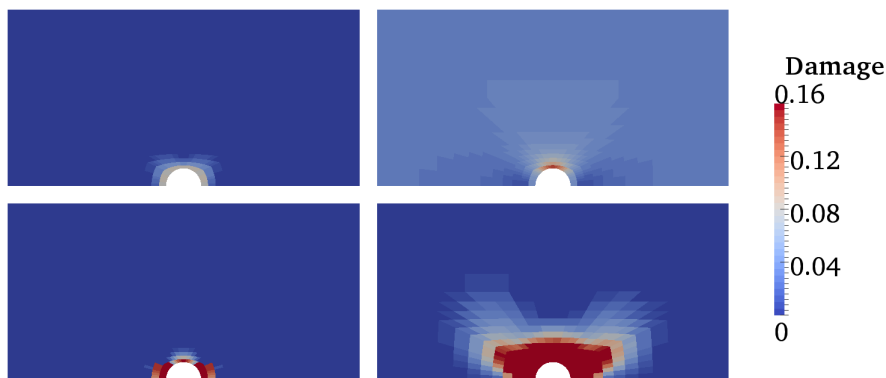


Figure 9. Damage at $t = 4000$ s for each initiation criterion in this work. From bottom-left moving clockwise, the criteria are: Drucker/Prager, maximum principal stress, energy measure, and Mazars/Pijauder-Cabot.

Figure 10 displays the permeability around the injection site for the Mazars/Pijauder-Cabot initiation criterion. Of the other criteria, the only one that showed permeability enhancement was the Drucker/Prager criterion and that was limited to the area immediately bordering the borehole. Figures 3 and 5 show that permeability enhancement does not occur until strain/damage values that are relatively close to the strain/damage at the peak load. With this type of definition, we would only expect to see permeability enhancement in the areas of the highest stress/strain (damage) in the specimen. The maximum principal stress and energy measure criteria did not show very high damage values (<0.16) due to their calibration with the compression data seen in Figure 4. Figure 11 (left) displays the damage for the Mazars/Pijauder-Cabot criterion with an initial horizontal flaw present near the borehole. Damage continues to propagate in the usual direction for the criterion, but additional damage occurs at the tip of the flaw. This additional damage is due to a combination of a stress concentration at the tip and additional cold water flowing down the flaw. Figure 11 (right) displays the thermal strain for this scenario. Thermal strain is present where the temperature has been reduced. However, the magnitude of the thermal strain is very small compared to the mechanical strain resulting from the *in situ* stress state. The flaw was represented by applying the damage variable equal to 0.8 in the elements that extended 10 mm to the right of the borehole. It is not clear that this is the best way to represent a single fracture with damage mechanics. This type of approach may be more appropriate for representing a network of connected micro-fractures in those elements.



Figure 10. Permeability values around injection well for the Mazars/Pijauder-Cabot initiation criterion. The area of enhanced permeability is localized around the injection site because permeability only increases at higher values of damage/strain as seen in Figures 3 and 5.

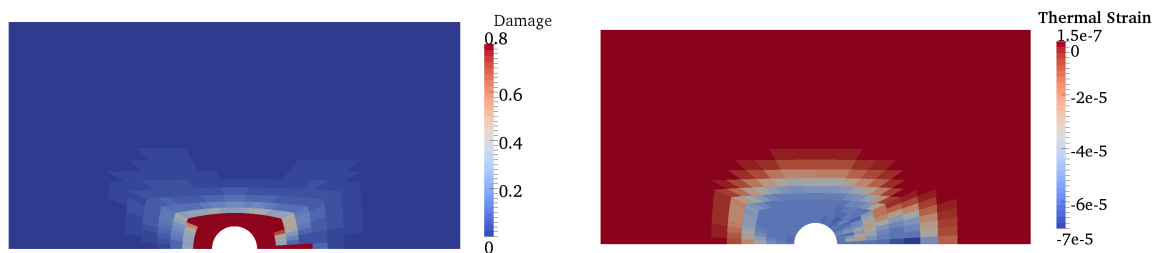


Figure 11. (Left): Damage around injection well for Mazars/Pijauder-Cabot criterion with an initial horizontal flaw of 10 mm. The flaw was described by setting damage = 0.8 in the elements extending from the right edge of the borehole. Damage continued to grow in the same direction as seen Figure 9, however additional damage occurred at the tip of the flaw. (Right): Thermal strain values associated with temperature changes in the rock from injecting cold water. The thermal strain values are approximately 3 orders of magnitude smaller than the mechanical strains due to the *in situ* stress-state in the material.

9. CONCLUSIONS AND FUTURE WORK

In this work we present a methodology and framework for the application of damage mechanics models to THM modeling for geothermal energy. We tested a number of popular initiation criteria and calibrated each model to the same stress-strain and permeability-strain plots. We found that the choice of initiation criterion can affect the result, sometimes significantly. This is a work in progress that we are continuing. It is not clear how any of these models will behave in a full 3-D reservoir simulation. We are working on coupling TOUGH2 with the ABAQUS for this investigation. As mentioned earlier, we are also in the process of investigating permeability enhancement relations that show some reduction in permeability (but with some permanent enhancement) when injection ceases. We are also investigating models similar to the work of Lu, *et al.* (2013) that approach damage mechanics as an actual representation of the microcracks in the domain. In those cases, material strains affect the initiation and propagation of microcracks, which affect material moduli, permeability, etc. We intend to extend those works by considering mode II (shear) opening in non-isothermal simulations. This work offers a simple framework for the investigation of multiple damage mechanics models and initiation criteria.

ACKNOWLEDGEMENTS

The authors wish to gratefully acknowledge GNS Science of New Zealand for their support of this project and thermal cracking simulation research at the University of Auckland.

REFERENCES

- Besson, J., Cailletaud, G., Chaboche, J., *et al.*: *Nonlinear Mechanics of Materials (Solid Mechanics and Its Applications)*, Springer, (2010).
- Bieniawski, Z.: Time-Dependent Behaviour of Fractured Rock, *Rock Mechanics*, **2**, (1970), 123-137.
- Bonet, J. and Wood, R.: *Nonlinear Continuum Mechanics for Finite Element Analysis*, Cambridge University Press, Cambridge, UK, (1997).
- Chen, W. and Han, D.: *Plasticity for Structural Engineers*, Gau Lih Book Co. Ltd., Taiwan, (1995).
- Cladouhos, T., Petty, S., Larson, B., Iovenitti, J., Levesay, B., and Baria, R.: Toward More Efficient Heat Mining: A Planned Enhanced Geothermal System Demonstration Project, *Geothermal Resources Council Transactions*, **33**, (2009).
- Clark, J.: A Hydraulic Process for Increasing the Productivity of Wells, *Transactions of Society of Petroleum Engineers of AIME*, **186**, (1949), 1-8.
- DeBorst, R., Crisfield, A., *et al.*: *Nonlinear Finite Element Analysis of Solids and Structures*, John Wiley and Sons Ltd, (2012).

- Dempsey, D., Kelkar, S., Lewis, K., *et al.*: Modeling Shear Stimulation of the Desert Peak EGS Well 27-15 Using a Coupled Thermal-Hydrological-Mechanical Simulator, *47th US Rock Mechanics/Geomechanics Symposium*, San Francisco, CA, USA (2013).
- Gangi, A.: Variation of Whole and Fractured Porous Rock Permeability with Confining Pressure, *International Journal of Rock Mechanics, Mineral Science, and Geomechanics*, **15**, (1978), 249-257.
- Halm, D. and Dragon, A.: A Model of Anisotropic Damage by Mesocrack Growth; Unilateral Effect, *International Journal of Damage Mechanics*, **5**, (1996), 384-402.
- Ingebritsen, S., Sanford, W., and Neuzil, C.: *Groundwater in Geologic Processes*. Cambridge University Press, New York. (2006).
- Kelkar, S., Lewis, K., Hickman, S., *et al.*: Modeling Coupled Thermal-Hydrological-Mechanical Processes During Shear Stimulation of an EGS Well, *Proceedings*, 37th Workshop of Geothermal Reservoir Engineering, Stanford University, Stanford, CA, (2012).
- Lee, H. and Cho, T.: Hydraulic Characteristics of Rough Fractures in Linear Flow under Normal and Shear Load, *Rock Mechanics and Rock Engineering*, **35 (4)**, (2002), 299-318.
- Lewis, R., and Schrefler, B.: *The Finite Element Method in the Static and Dynamic Deformation and Consolidation of Porous Media*, John Wiley and Sons, (1998).
- Lu, Y., Elsworth, D., and Wang, L.: Microcrack-based Coupled Damage and Flow Modeling of Fracturing Evolution in Permeable Brittle Rocks, *Computers and Geotechnics*, **49**, (2013), 226-244.
- Mazars, J. and Pijaudier-Cabot, G.: Continuum Damage Theory – Application to Concrete, *ASCE Journal of Engineering Mechanics*, **115**, (1989), 345-365.
- Nathenson, M.: The Dependence of Permeability on Effective Stress from Flow Tests at Hot Dry Rock Reservoirs at Rosemanowes (Cornwall) and Fenton Hill (New Mexico), *Geothermics*, **28**, (1999), 315-340.
- Pogacnik, J., Leary, P., and Malin, P.: Physical/Computational Framework for EGS *in situ* Fracture Stimulation, *Proceedings*, New Zealand Geothermal Workshop, (2012).
- Rutqvist, J., Dobson, P., Garcia, J., *et al.*: Pre-Stimulation Coupled THM Modeling Related to the Northwest Geysers EGS Demonstration Project, *Proceedings*, 38th Workshop of Geothermal Reservoir Engineering, Stanford University, Stanford, CA (2013).
- Tang, C., Tham, L., Lee, P., *et al.*: Coupled Analysis of Flow, Stress, and Damage (FSD) in Rock Failure, *International Journal of Rock Mechanics and Mining Sciences*, **39**, (2002), 477-489.
- Voyiadjis, G. and Kattan, P.: *Damage Mechanics*, CRC Press, Boca Raton, FL, USA, (2005).
- Wang, J. and Park, H.: Fluid Permeability of Sedimentary Rocks in a Complete Stress-Strain Process, *Engineering Geology*, **63**, (2002), 291-300.
- Witherspoon, P., Wang, J., *et al.*: Validity of Cubic Law for Fluid Flow in a Deformable Rock Fracture, *Water Resources Research*, **16 (6)**, (1980), 1016-1024.
- Zhang, R., Jiang, Z., Sun, Q., and Zhu, S.: The Relationship Between the Deformation Mechanism and Permeability of Brittle Rock, *Natural Hazards*, **66**, (2013), 1179-1187.
- Zhou, J. Shao, J., Xu, W.: Coupled Modeling of Damage Growth and Permeability Variation in Brittle Rocks, *Mechanics Research Communications*, **33**, (2006), 450-459.